Çaha, I., Alves, A., Chirico, C., Pinto, A., Tsipas, S., Gordo, E. & Toptan, F. (2020). Corrosion and Tribocorrosion Behavior of Ti-40Nb and Ti-25Nb-5Fe Alloys Processed by Powder Metallurgy. *Metallurgical and Materials Transactions A*, 51(6), pp. 3256–3267.

DOI: 10.1007/s11661-020-05757-6

Corrosion and Tribocorrosion Behavior of Ti-40Nb and Ti-25Nb-5Fe Alloys Processed by Powder Metallurgy

IHSAN ÇAHA, ALEXANDRA ALVES, CATERINA CHIRICO, ANA PINTO, SOPHIA TSIPAS, ELENA GORDO, and FATIH TOPTAN

The requirement of good mechanical properties, lower Young's modulus, superior corrosion resistance, and excellent biocompatibility makes β-type titanium alloys attractive materials for orthopedic implants. In this study, Ti-25Nb-5Fe and Ti-40Nb β-type titanium alloys were designed and produced by powder metallurgy route using titanium hydride, niobium, and iron powders. The effect of sintering conditions on microstructure, corrosion, and tribocorrosion behavior was explored. Electrochemical behavior was investigated in saline solution (9 g/L NaCl) at body temperature by using potentiodynamic polarization and electrochemical impedance spectroscopy. Tribocorrosion behavior was evaluated by reciprocating against an alumina ball at open circuit potential, as well, under anodic and cathodic potentiostatic conditions in saline solution (9 g/L NaCl) at body temperature. The physical, electrochemical, and tribo-electrochemical behaviors of both alloys were improved with increasing sintering time at 1250 °C from 2 to 4 hours and decreasing Fe particle size for Ti-25Nb-5Fe alloy. Degradation under tribocorrosion conditions was mainly governed by mechanical wear on Ti-25Nb-5Fe alloy; however, Ti-40Nb alloy exhibited an antagonistic effect between corrosion and wear during testing under anodic applied potential due to the formation of a denser tribolayer.

I. INTRODUCTION

Ti and its alloys have attracted attention in biomedical field due to their good corrosion resistance, high biocompatibility, lower Young's modulus as compared to stainless steel and CoCrMo, and superior mechanical properties. Although α-type commercially pure Ti (cp-Ti) and $\alpha + \beta$-type Ti-6Al-4V alloy s are commonly employed for implants, they exhibit some clinical concerns. As reviewed by Niinomi and Nakai,[1] the Young's modulus of cp-Ti and $\alpha + \beta$-type Ti-6Al-4V alloy (~ 110 GPa) is much higher than that of bone (20 GPa for cortical bone), which leads to the stress-shielding effect caused by the mismatch in Young's modulus between the implant and surrounding bone, eventually resulting in bone resorption and aseptic implant loosening. Moreover, as the most popular Ti alloy, Ti-6Al-4V alloy has raised concerns as a result of Al and V ion release that may cause adverse effects on tissues. For instance, Hallab *et al.*[2] reported that Al and V ions reduced proliferation, viability, and affected the morphology of human peri-implant cells (osteoblast, fibroblasts, and lymphocytes). Therefore, β-type Ti alloys have gained attention due to their composition having non-toxic and allergy free β stabilizer elements including Nb, Zr, Mo, Ta as reported by Okazaki *et al.*,[3] better corrosion resistance compared to cp-Ti as shown by Bai *et al.* for β-type Ti-45Nb alloy,[4] and also lower Young's modulus as reviewed by Gepreel and Niinomi[5] for different β-type Ti alloys.

Fang *et al.*[6] has recently reviewed powder metallurgy (P/M) of Ti and pointed the limitation on implant fabrication by melt-wrought techniques due to high cost, complex fabrication, and subsequent machining processes where P/M offers an attractive alternative to

IHSAN ÇAHA and ALEXANDRA ALVES are with the CMEMS-UMinho - Center for MicroElectroMechanical Systems, Universidade do Minho, Azurém, 4800-058 Guimarães, Portugal. Contact e-mail: ihsancaha@gmail.com; CATERINA CHIRICO is with the Universidad Carlos III de Madrid, Avda. Universidad, 30, 28911 Leganés, Spain; ANA PINTO is with the CMEMS-UMinho - Center for MicroElectroMechanical Systems, Universidade do Minho and also with the Universidade do Minho, Dept. Eng. Mecânica, Azurém, 4800-058 Guimarães, Portugal; SOPHIA TSIPAS and ELENA GORDO are with the Universidad Carlos III de Madrid and also with the Instituto "Álvaro Alonso Barba", 30, 28911 Leganés, Madrid, Spain; FATIH TOPTAN is with the CMEMS-UMinho - Center for MicroElectroMechanical Systems, Universidade do Minho and also with the Universidade do Minho, Dept. Eng. Mecânica and also with the IBTN/Br Brazilan Branch of the Institute of Biomaterials, Tribocorrosion and Nanomedicine, 17033-360 Bauru, SP, Brazil.

enable near-net-shape processing with adjusted chemical composition, or even porosity, that is known to be favorable for biological response and for further reduction on Young's modulus.

According to a review by Niinomi *et al.*,[7,8] among the β-type Ti alloys, Ti-Nb-based alloys have been the most studied system not only due to their mechanical properties and biocompatibility, but also due to their good corrosion resistance. For instance, the Ti-20Nb-10Zr-5Ta alloy was presented a promising material due to combined properties of low Young's modulus, very low corrosion rate, and good biocompatibility.[9] Accordingly, Bai *et al.*[4] studied the electrochemical behavior of Ti-45Nb alloy in different electrolytes including simulated body fluid and artificial-saliva-based solutions and reported a better response as compared to cp-Ti. However, load-bearing biomedical implants not only suffer to corrosion, but also suffer to tribocorrosion since they are subjected to relative movements in corrosive environments (body fluids) of the human body. Limited studies are available in the literature on the tribocorrosion behavior of β-type Ti alloys. Correa *et al.*[10] compared the tribocorrosion behavior of Ti-15Zr-xMo (x = 7.5 and 15) alloys with cp-Ti by performing tests under 1.5 N load, 2 Hz sliding frequency against 10 mm diameter alumina ball in simulated body fluid and reported lower corrosion tendency under sliding, as well as improved repassivation behavior as compared to cp-Ti. Pina *et al.*[11] studied the tribocorrosion behavior of P/M Ti-30Nb-xSn (x = 0, 2, and 4) Ti alloys in phosphate buffered saline against 6 mm diameter alumina ball under 5 N and reported increased mechanically activated corrosion after Sn addition due to elevated dissolution rate. More *et al.*[12] studied tribocorrosion behavior of β-type (Ti-12.5Mo, Ti-13Nb-13Zr, and Ti-29Nb-13Ta-4.6Zr) and $\alpha + \beta$-type (Ti-6Al-4Fe) alloys against ultra-high molecular weight polyethylene (UHMWPE) in Hank's balanced salt solution with and without incorporation of some synovial fluid constituents under relatively lower contact pressures of 34 to 35 MPa. The authors reported only a very weak tribo-electrochemical influence for the alloys whereas the wear of UHMWPE counter-material was governed by the adhered third bodies on the surfaces.

Regarding the literature, Ti-40Nb alloy presents an appropriate combination of promising properties in Ti-Nb binary alloys for implants. Calin *et al.*[13] reported the Young's modulus of casted and heat-treated Ti-40Nb alloy as 69 GPa. Helth *et al.*[14] investigated the adhesion and spreading of human mesenchymal stromal cell on cp-Ti and Ti-40Nb alloy and reported more pronounced behavior for Ti-40Nb alloy. On the other hand, Fe has gained attention as β stabilizer in Ti due to its non-toxicity and low cost (particularly compared to Nb). Chaves *et al.*[15] explored the microstructural properties and mechanical behavior of β-type Ti-(10, 15, and 25)Nb-3Fe alloys and reported that Ti-25Nb-3Fe alloy exhibited improved phase stability and the lowest Young's modulus (65 GPa). Mohan *et al.*[16] produced Ti-12Mo-6Zr-xFe (x = 1, 2, 3, and 4) alloys by P/M and reported that additions of small amounts of Fe improved the β-phase stability. Apart from structural and mechanical properties, biological response of cast Ti-5Nb-xFe (x = 0, 1, 2, 3, 4, and 5) alloys was investigated by Hsu *et al.*[17] where all studied alloys were reported as biocompatible. Ehtemam-Haghighi *et al.*[18] investigated the wear behavior of Ti-xNb-7Fe (x = 0, 1, 4, 6, 9, and 11) alloys sliding against a stainless steel disc in ambient atmospheric condition under 25 N normal load and indicated that the increasing amount of Nb decreased the hardness/Young's modulus ratio resulting in increased wear rate.

In the last decade, different β-type Ti alloys have been developed for biomedical applications; however, their degradation behavior is yet to be fully understood. Since degradation has been reported as one of the main reasons of early revision of hip implants resulted from breakdown and depassivation of passive film due to relative micro-motions, leading to the release of metallic ions and wear products to around tissues,[19,20] this work aimed to study the degradation behavior of Ti-40Nb and Ti-25Nb-5Fe alloys produced by P/M, with diverse electrochemical and tribo-electrochemical tests. Ti-xNb-5Fe system was proposed with small addition of Fe and the value of x was theoretically simulated to obtain a similar β phase fraction to that in Ti-40Nb alloy.

II. MATERIAL AND METHODS

A. *Materials and Design of Novel Ti Alloys*

Commercial TiH_2 (GfE, D_{50}: 27 μm), Nb (Alfa Aesar, D_{50}: 15 μm), and two kinds of Fe powders with a coarse particle size (Pomenton, D_{50}: 34 μm) and with a finer particle size (H.C. Starck, D_{50}: 4 μm) were used as raw material. Specifically, two P/M Ti alloys were designed as Ti-40Nb and Ti-25Nb-5Fe. Ti-40Nb was considered as starting composition and the Thermocalc software was used to assess the fraction of β phase by simulation of Ti-Nb phase diagram. In order to obtain the highest β phase fraction together with decreasing Nb percentage, Ti-x*Nb*-5Fe system was also studied. The necessary amount of Nb was simulated by the same software to achieve a similar β phase fraction to that of Ti-40Nb alloy at the same temperature (400 °C) on Ti-Nb-Fe phase diagram and Ti-25Nb-5Fe composition was defined.

B. *Processing*

Two different mixtures containing Ti-40Nb and Ti-25Nb-5Fe (in weight percentage) were homogenized by mixing in a multi-directional mixer (Turbula®) for 1 hour. The mixtures were prepared with TiH_2 as a raw material to obtain the designed final compositions after dehydrogenization. The samples (14 mm in diameter and about 4 mm in height) were obtained under 700 MPa constant pressure following the compaction procedure previously explained elsewhere.[21] The samples were sintered under high vacuum (10^{-5} mbar) in a tubular furnace by following Cycle 1 and Cycle 2

(Figure 1) and the samples were labeled as c1 and c2, respectively. Preliminary studies (data not shown) showed that Ti-25Nb-5Fe alloy produced with coarser Fe particles by following the c2 sintering cycle presented fully β phase, but it did not present a reduction on porosity (6.1 ± 0.6 pct). Therefore, Ti-25Nb-5Fe c2 group of samples were processed with finer Fe particles.

Prior to structural characterization, samples were grounded with SiC papers down to 1000 mesh size and mirror finished by using OPS (colloidal silica with particle size of 0.06 μm). Finally, the samples were placed in an ultrasonic bath, cleaned with propanol for 10 minutes and rinsed with distilled water for 5 minutes.

For corrosion and tribocorrosion tests, the samples were ground by SiC papers down to 1200 mesh size. Afterwards, the samples were cleaned by following the previously described procedure and held up in a desiccator for 1 day before starting each test. All tests were repeated at least three times in order to ensure the reproducibility and the results were given as the arithmetic mean ± standard deviation.

C. *Corrosion Tests*

Corrosion tests were carried out in a three electrode electrochemical cell (adapted from ASTM: G3-89) having a saturated calomel electrode (SCE) as reference electrode (RE), a Pt electrode as counter electrode (CE), and the samples having 0.38 cm^2 of exposure area as working electrode (WE), connected to Gamry Potentiostat/Galvanostat/ZRA (model Reference 600+). Electrochemical impedance spectroscopy (EIS) and potentiodynamic polarization tests were performed in a saline solution (9 g/L NaCl), as a simple physiological solution, at 37 ± 2 °C temperature. The open circuit potential (OCP) was monitored for the stabilization of native oxide film on the alloy surfaces and afterwards EIS tests were performed at OCP with a frequency range between 10^{-2} to 10^{5} Hz with 7 points per frequency decade and 10 mV amplitude of sinusoidal signal. After EIS test, potentiodynamic polarization test was employed with 0.5 mV/s scanning rate from − 0.25 V_{OCP} up to 1.5 V_{SCE} in anodic direction.

D. *Tribocorrosion Tests*

Tribocorrosion tests were performed in a tribo-electrochemical cell located in a reciprocating ball-on-plate tribometer (CETR-UMT-2) and connected to a potentiostat (Gamry, Potentiostat/Galvanostat/ZRA model Reference 600) with three electrode configurations that used in the corrosion tests. The experiments were carried out in 30 ml of saline solution (9 g/L NaCl) at 37 ± 2 °C against an alumina ball (Ceratec, 10 mm in diameter). Tribological parameters were chosen as 1 N normal load, 1 Hz frequency, 3 mm of total stroke length, and 30 minutes of sliding time. Tests were performed under OCP, as well, under anodic (+ 0.5 V_{SCE}) and cathodic (− 0.3 V_{OCP}) potentiostatic conditions, to study the interplay between corrosion and wear. The anodic potential was selected as a potential corresponding to the passive region whereas the cathodic potential was selected considering the susceptibility of Ti alloys to hydrogen absorption and consequent embrittlement that observed as an *in vivo* mechanism by Rodrigues *et al.*[22] for retrieved Ti alloy hip implants.

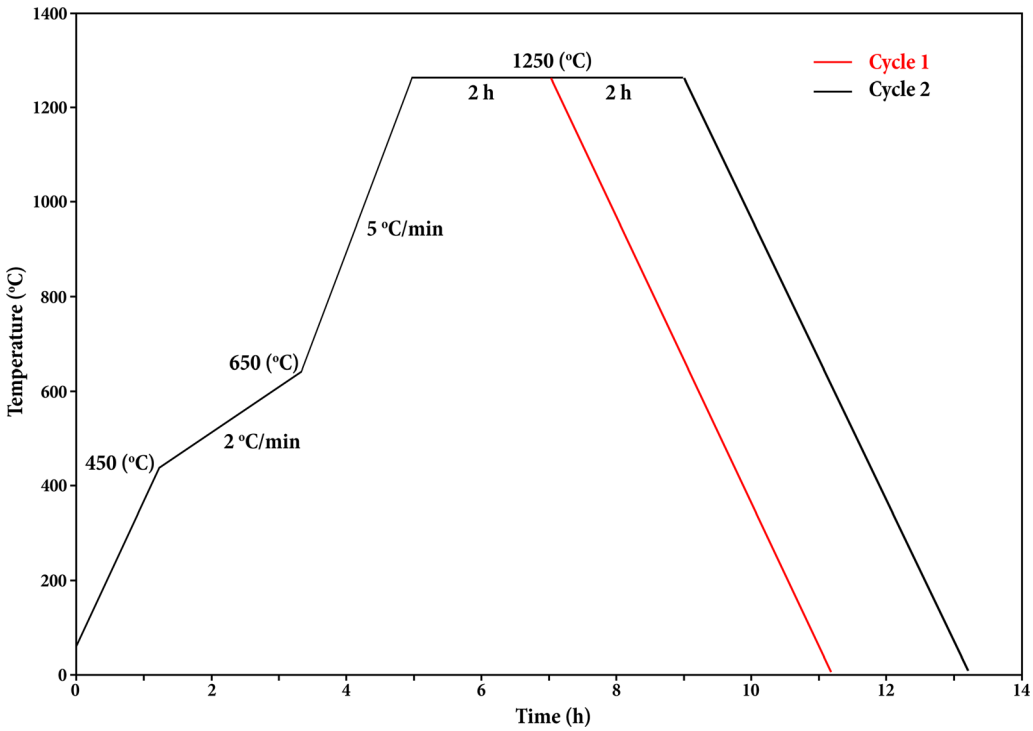

Fig. 1—Sintering cycles.

E. *Characterization*

Porosity (P_{Total}) was estimated according to Eq. [1] where ρ_s and ρ_{th}correspond to the bulk-sintered and theoretical density, respectively. The ρ_s was obtained by the geometrical approach and the ρ_{th} was calculated through the rule of mixtures. The ρ_{th} of Ti was considered as 4.51 g/cm^3 and complete dehydrogenation of TiH_2 was assumed.

$$P_{Total} = \left(1 - \frac{\rho_s}{\rho_{th}}\right) \times 100 \quad [1]$$

Hardness was attained by microindentation measurements under 0.5 N load and 20 seconds dwelling time using a microhardness tester (Zwick Roell, model ZHVμ) over three samples with at least 10 indentations for each one.

Microstructures were evaluated by scanning electron microscope (SEM, Phillips XL-30) and structural analysis was performed by X-ray diffraction (XRD, X'pert Phillips diffractometer with Cu-Kα radiation of 1.54 Å and 40 kV). The phase percentages were calculated by following Eq. [2], where I is the intensity.

$$\text{Pct phase}_\alpha = \frac{\sum I_{\alpha \text{ peaks}}}{\sum I_{\text{all peaks}}} \quad [2]$$

Table I. Porosity and Hardness Values

Samples	Porosity (pct)	Hardness ($HV_{0.05}$)
Ti-40Nb c1	5.1 ± 0.3	228 ± 19
Ti-40Nb c2	4.5 ± 1.6	243 ± 40
Ti-25Nb-5Fe c1	4.9 ± 0.3	284 ± 14
Ti-25Nb-5Fe c2	1.0 ± 0.7	310 ± 15

After tribocorrosion tests, samples were cleaned with abovementioned procedures and the worn surfaces were analyzed by using field emission gun (SEM FEI Nova 200) equipped with energy dispersive spectrometer (EDS, EDAX - Pegasus X4M). Wear volume loss was calculated over the 2D profiles obtained by a contact profilometer (Veeco, Dektak 150) using the model and the methodology previously described by Doni *et al.*[23]

III. RESULTS

A. *Physical Properties and Microstructure*

Porosity and hardness values of samples are given in Table I. Both alloys presented lower average values of porosity on the c2 condition where the difference was more pronounced on Ti-25Nb-5Fe alloy.

According to the XRD spectra (Figure 2), all samples were mainly constituted of β-Ti, however, Nb peaks found on Ti-40Nb samples showing undiffused Nb on this alloy. According to Eq. [2], Ti-40Nb c1 was composed of 2.4 pct α-Ti, 91.1 pct β-Ti, and 6.5 pct Nb, while Ti-40Nb c2 was composed of 94.5 pct β-Ti and 5.5 pct Nb. Also, it can be seen that more α-Ti phase transformed to β-Ti phase and the percentage of Nb decreased with c2 for Ti-40Nb alloy. Ti-25Nb-5Fe alloys presented entirely β-Ti phase.

BSE-SEM images for both alloys and processing conditions are given in Figure 3. Both alloys presented predominantly β-Ti microstructure; however, backscattering electrons revealed some areas rich in Nb (bright spots) for Ti-40Nb alloy, as in accordance with the XRD results. Since Fe addition improved the diffusion processes between Nb and Ti, Nb-rich bright spots were not observed on Ti-5Fe-25Nb alloy. On the other hand, although total porosity was similar between two alloys produced at c1, bigger pores were observed on

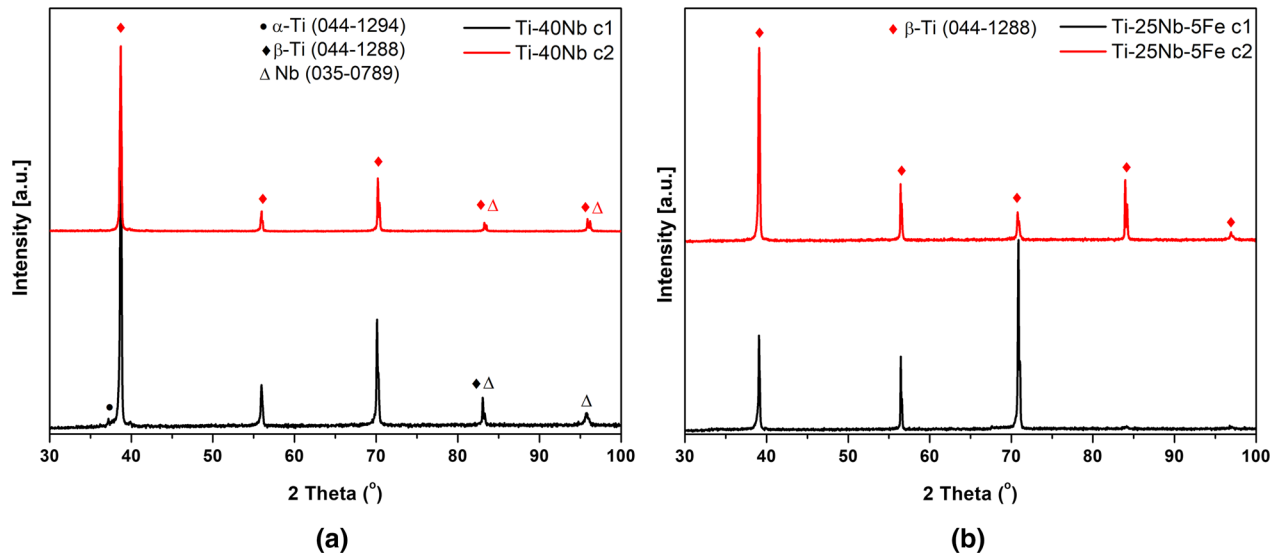

Fig. 2—XRD spectra of (*a*) Ti-40Nb and (*b*) Ti-25Nb-5Fe alloys for both processing conditions.

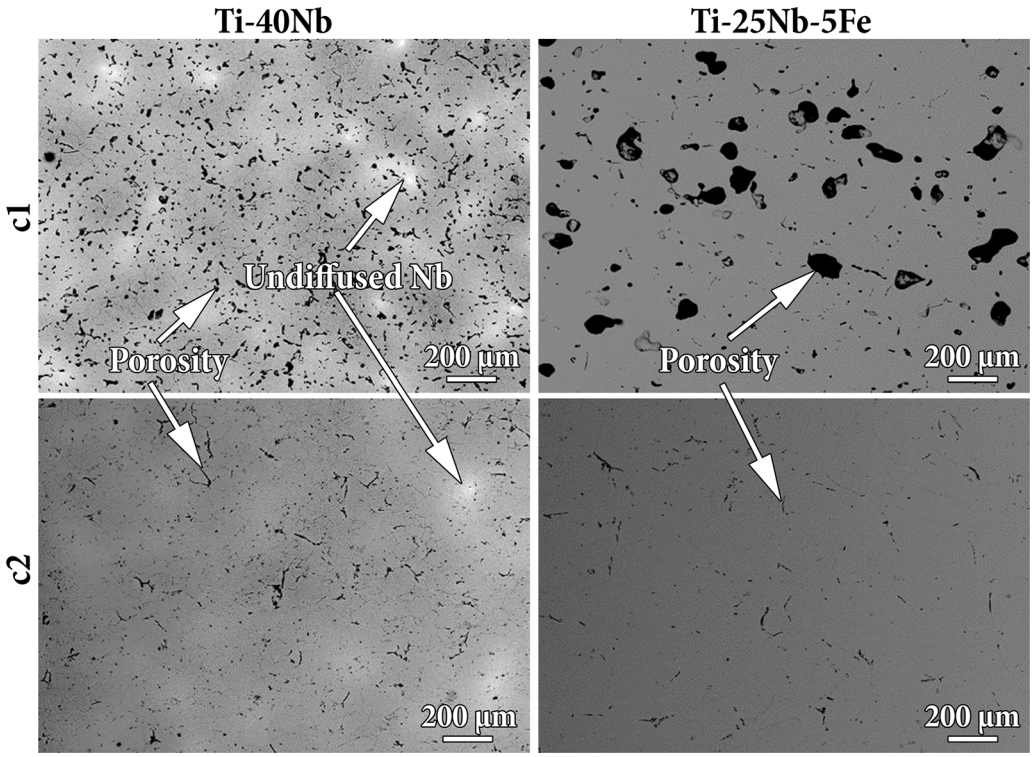

Fig. 3—BSE-SEM images of Ti-40Nb and Ti-25Nb-5Fe alloys for c1 and c2 conditions.

Ti-5Fe-25Nb alloy. After processing under c2, both alloys presented lower porosity and similar pore size.

B. *Corrosion Behavior*

Representative potentiodynamic polarization curves for all samples are given in Figure 4, extracted values of passivation current density (i_{pass}) and corrosion potential ($E_{(i=0)}$) are presented in Table II. All samples presented well-defined passivation plateaus started at average 0, 260, 200, and 380 mV_{SCE} for Ti-40Nb c1, Ti-40Nb c2, Ti-25Nb-5Fe c1, and Ti-25Nb-5Fe c2, respectively. The results indicated that Ti-25Nb-5Fe samples showed slightly higher average $E_{(i=0)}$ and lower average i_{pass} values as compared to Ti-40Nb samples. The same trend was also observed on both alloys processed under c2, in comparison with the alloys processed under c1.

The representative Bode diagram of EIS spectra is given in Figure 5(a). The constant values of $|Z|$ and near 0 deg phase angle were observed at the high-frequency range (10^3 to 10^5 Hz) owing to the electrolyte resistance. Near − 90 deg of phase angle values in the medium and low ranges of frequency indicated the typical capacitive behavior of a passive oxide film. The phase angle values in medium frequency range were decreased and the $|Z|$ values in low frequency range were increased for both alloys processed under c2.

The electrical equivalent circuit (EEC) with one-time constant, modified Randles circuit, is used to simulate the EIS experimental data by using Echem Analyst software as shown in Figure 5(b) and the EEC

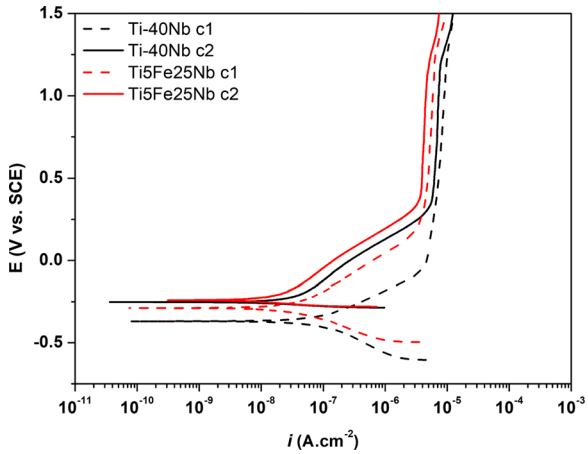

Fig. 4—Potentiodynamic polarization curves for Ti-40Nb and Ti-25Nb-5Fe alloys.

parameters are given in Table III. The EEC includes R_e, R_{ox}, and Q_{ox} corresponding to an electrolyte resistance, the resistance of the oxide film, and a constant phase element (CPE), respectively. The CPE, demonstrating a shift from an ideal capacitor was used in the EEC. The impedance of a CPE is defined as $Z_{CPE} = [Y_0(j\omega)^n]^{-1}$, where Y_0 is the admittance of CPE, ω is the angular frequency, $j = \sqrt{-1}$ is the imaginary number, and n *is* the exponential factor, $-1 \le n \le 1$. When n value is 1, 0, and − 1, the CPE response is an ideal capacitor, a resistor, and an inductor, respectively. The n

value is associated with surface heterogeneities and roughness. The C_{ox} values converted from Q_{ox} values through Eq. [3] derived from Brug's equation;

$$C_{ox} = \left[Q_{ox} R_e^{(1-n)}\right]^{\frac{1}{n}} \quad [3]$$

The quality of fitting on the EEC was assessed by the goodness of fitting where the proposed model showed values below 10^{-3} (Table III). According to these values, the C_{ox} values only slightly decreased from Ti-40Nb to Ti-25Nb-5Fe; however, Ti-25Nb-5Fe exhibited noticeably higher R_{ox} values. When two processing conditions were compared, no clear trend was observed on R_{ox}, but relatively lower C_{ox} values were observed on both alloys processed under c2. Moreover, both alloys presented very similar n values whereas the values were noticeably higher on both alloys processed under c2.

C. *Tribocorrosion Behavior*

1. *Tribocorrosion at OCP*

The OCP evolution before, during, and after sliding, together with the corresponding COF values are presented in Figure 6. When sliding started, values of OCP dropped abruptly for all samples indicating a damage given to the passive film by the exposure of the bare metal (worn area) to the electrolyte. After sliding, the values immediately increased approximately near to the values obtained before sliding owing to spontaneous repassivation. During sliding, the average OCP values obtained from three tests for Ti-40Nb c1, Ti-40Nb c2, Ti-25Nb-5Fe c1, and Ti-25Nb-5Fe c2 samples were -622 ± 71 mV_{SCE}, -510 ± 59 mV_{SCE}, -589 ± 39 mV_{SCE}, and -511 ± 19 mV_{SCE}, respectively, indicating relatively more positive values for c2 for both alloys. COF values presented a relatively stable evolution for all samples. The average COF values of Ti-40Nb c1, Ti-40Nb c2, Ti-25Nb-5Fe c1, and Ti-25Nb-5Fe c2 samples were 0.71 ± 0.003, 0.61 ± 0.10, 0.64 ± 0.12, and 0.54 ± 0.03, respectively, where slightly lower values obtained on Ti-25Nb-5Fe alloy and decreased values were observed for both alloys processed under c2.

Table II. Corrosion Potential ($E_{(i\ =\ 0)}$) and Passivation Current Density (i_{pass}) Values for Ti-40Nb and Ti-25Nb-5Fe Alloys

	$E_{(i\ =\ 0)}$ (mV_{SCE})	i_{pass} ($\mu A\ cm^{-2}$)
Ti-40Nb c1	-359 ± 9	8.28 ± 0.84
Ti-40Nb c2	-280 ± 33	6.58 ± 0.78
Ti-25Nb-5Fe c1	-289 ± 14	5.00 ± 0.55
Ti-25Nb-5Fe c2	-229 ± 22	4.03 ± 0.16

2. *Tribocorrosion at applied potentials*

In order to investigate the interactions between wear and corrosion, tribocorrosion tests were performed under anodic (AP) and cathodic (CP) applied potentials to simulate the degradation due to wear/corrosion and mechanical wear, respectively. Figure 7 presents the anodic current evolution before, during, and after sliding at an applied potential of + 0.5 V_{SCE}, as well, the corresponding COF values. Before sliding, the current density values were stable due to the presence of a stable oxide film formed on the surfaces. Under sliding, the current evolution of Ti-40Nb was significantly different than Ti-25Nb-5Fe for both c1 and c2 conditions. When sliding started, Ti-40Nb c1 and Ti-40Nb c2 presented only a very small increase on current density than remained relatively stable around these values for around 2 and 5 minutes, respectively. Afterwards, sharp increases on current density were observed for both samples then the values decreased

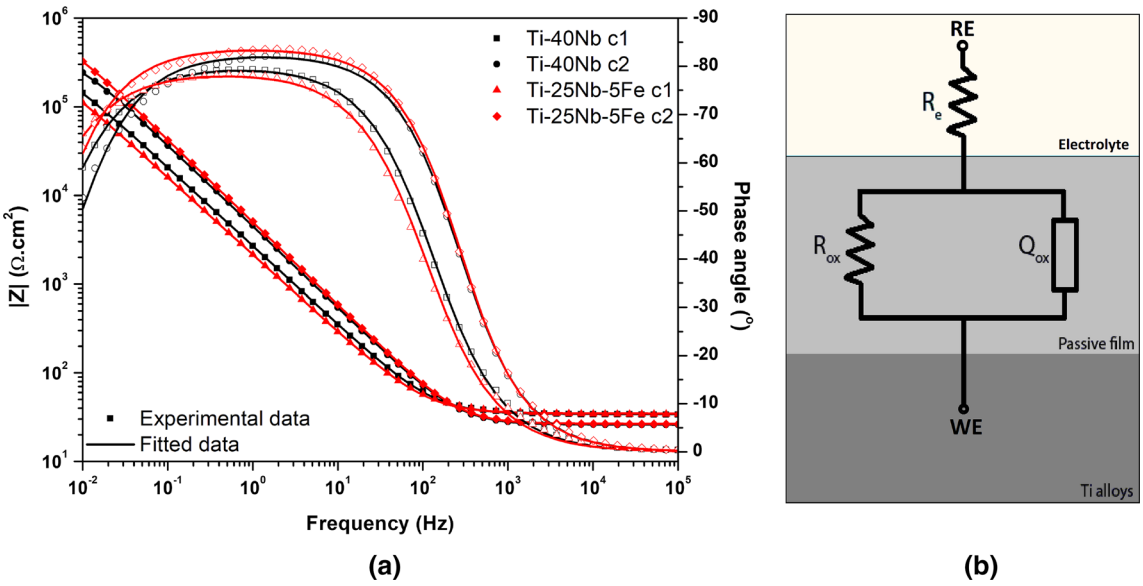

Fig. 5—Bode diagram (*a*) and EEC (*b*) of Ti-40Nb and Ti-25Nb-5Fe alloys.

Table III. Electrochemical Parameters Obtained from the Proposed EEC

Sample	R_{ox} ($\times 10^5$ Ω cm^2)	C_{ox} (μF cm^{-2})	n	χ^2 ($\times 10^{-4}$)
Ti-40Nb c1	3.5 ± 0.7	39.4 ± 12.4	0.88 ± 0.03	4.4 ± 2.7
Ti-40Nb c2	3.8 ± 0.9	26.0 ± 4.8	0.92 ± 0.01	3.2 ± 0.3
Ti-25Nb-5Fe c1	9.0 ± 2.9	33.0 ± 9.4	0.88 ± 0.01	5.5 ± 4.0
Ti-25Nb-5Fe c2	8.4 ± 0.5	21.2 ± 2.4	0.93 ± 0.01	2.2 ± 0.8

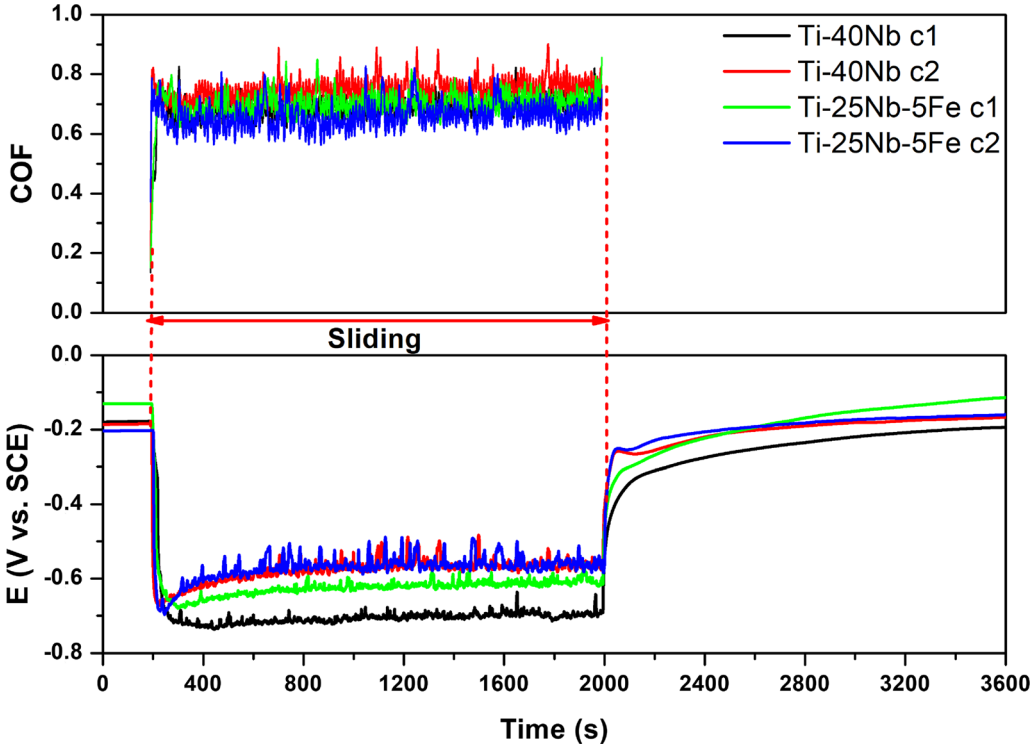

Fig. 6—Tribocorrosion at OCP: evolution of OCP together with corresponding COF values.

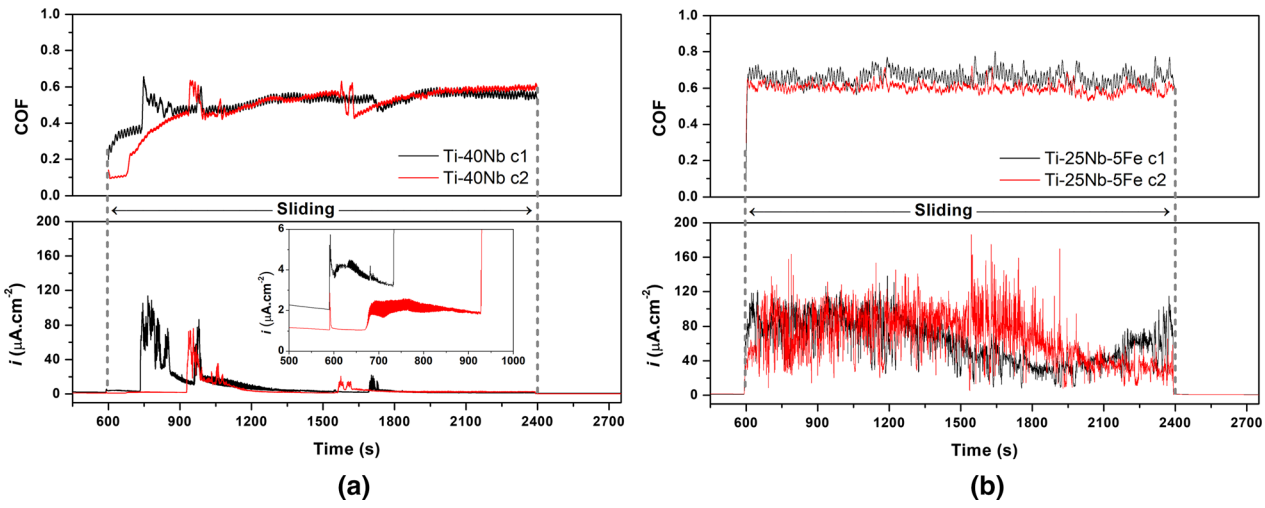

Fig. 7—Tribocorrosion at anodic applied potential: evolution of current density together with corresponding COF values for (*a*) Ti-40Nb and (*b*) Ti-25Nb-5Fe alloys.

close to the values recorded on the onset of the sliding. Regarding Ti-25Nb-5Fe samples, larger current density values were recorded during all sliding period as compared to Ti-40Nb alloy. When the counter-material unloaded, the current density fell for all samples to the values close to the ones recorded before sliding indicating the repassivation of the worn track area. Also, the anodic charge, Q, was estimated through integration of the current curves over sliding time. The Q values of Ti-40Nb c1, Ti-40Nb c2, Ti-25Nb-5Fe c1, and Ti-25Nb-5Fe c2 samples were calculated as $2.1 \times 10^{-2} \pm 0.09 \times 10^{-2}$, $1.2 \times 10^{-2} \pm 0.3 \times 10^{-2}$, $11.8 \times 10^{-2} \pm 1.1 \times 10^{-2}$, and $10.8 \times 10^{-2} \pm 2.7 \times 10^{-2}$ coulombs, respectively. Ti-25Nb-5Fe samples presented approx. 10 times higher Q values than Ti-40Nb alloys for both c1 and c2 conditions, indicating significantly higher corrosion kinetics under sliding. When Q values obtained for both processing conditions are compared, although some small decreases were obtained for the c2 condition, considering the standard deviation values, no obvious difference can be pointed.

In case of Ti-40Nb samples, when sliding started, COF values were gradually increased till the corresponding current density values decreased close to the ones observed on the onset of sliding, afterwards, remained relatively stable during the remaining sliding period. However, when an increase occurred on the current density values, larger fluctuations were detected on the corresponding COF values. Regarding Ti-25Nb-5Fe alloys, when the sliding started, COF values were suddenly increased up to the values around 0.64 ± 0.02 and 0.62 ± 0.05 for Ti-25Nb-5Fe c1 and Ti-25Nb-5Fe c2, respectively, and then evolved around these values till the end of sliding.

3. *Wear morphology*

SEM images of surfaces worn under OCP, AP, and CP are given in Figure 8. All worn surfaces presented typical wear surface morphologies known for Ti and Ti alloys, most predominantly, parallel ploughing grooves and abrasion scratches, together with a discontinuous tribolayer (oxidized patches) particularly for the samples tested under OCP and AP as also previously had been reported by Silva *et al.*[24] for Ti, by Runa *et al.*[25] for Ti-6Al-4V, and by Correa *et al.*[10] for Ti-15Zr-xMo (x = 7.5 and 15). Discontinuous tribolayer appeared to be denser on the Ti-40Nb alloys tested under AP conditions, as evidenced on BSE images with darker regions.

Figure 9 shows the SEM images of the worn alumina ball surfaces (counter-material) together with the respective EDS spectra. The visible wear damage on balls worn against Ti-40Nb alloy tested at AP condition were less severe for both processing conditions. Transferred material from samples to the counter-material was confirmed by EDS analysis for all conditions where lower visible amount of transferred material was observed on the balls slid against Ti-40Nb alloy at AP condition.

Figure 9 shows SE-SEM images and respective EDS spectra of the alumina ball surfaces worn against Ti-40Nb c1, Ti-40Nb c2, Ti-25Nb-5Fe c1, and Ti-25Nb-5Fe c2 tested under OCP, AP, and CP.

Figure 10 shows representative profiles taken from the center of the wear tracks, together with the total wear volume loss values. Ti-25Nb-5Fe exhibited relatively lower average wear volume loss under OCP and CP; however, clearly, the opposite trend was observed for AP. Regarding the tribo-electrochemical testing conditions, Ti-25Nb-5Fe alloys exhibited similar values for all conditions whereas the wear volume loss values for Ti-40Nb alloys decreased from OCP to AP where the effect of cathodic polarization was relatively small, but the effect of anodic polarization was clearly predominant. On the other hand, within the same alloys, no clear effect of processing conditions on the wear loss was observed.

IV. DISCUSSION

A. *Physical Properties*

The microstructure, porosity, hardness, and phase distribution were significantly influenced by sintering conditions. Guo *et al.*[26] indicated that the decreasing porosity for Ti-24Nb-4Zr-7.9Sn alloy with increasing holding times in 1250 °C was due to the β grain coarsening and the dissolution of prior α phases in the β matrix, which might also be the reason for decreasing porosity on c2 condition. The results pointed that Fe addition increased the hardness, and also the hardness of both alloys slightly increased when processed under c2 condition. As pointed out by Sharma *et al.,*[27] the hardness increased with the increasing sintering time due to more homogenous distribution of the phases in its microstructure. Ti-25Nb-5Fe alloy presented fully β phase for both conditions due to the well-known β stabilizing effect of Fe, which was reported by Niinomi *et al.*[28] as a one of the most effective β stabilizer element. According to John,[29] the atomic radius of Fe (1.24 Å) is smaller than Ti (1.45 Å) and Nb (1.43 Å). The peaks of Ti-25Nb-5Fe were shifted to right due to the decrease on the lattice parameters of the β phase. The (110) peak at 2θ = 38.5 deg, representing body-centered cubic (bcc) structure, became most intense and two additional β peaks were observed with c2 condition as result of a longer sintering stage.

B. *Corrosion Behavior*

The potentiodynamic polarization and EIS results indicated that increased sintering time may lead to formation of a more stable and protective oxide film in contact with NaCl solution, leading to an improved corrosion performance. Although all tested samples presented similar corrosion mechanism, as represented by the same EEC, Ti-25Nb-5Fe alloy presented better corrosion resistance and lower corrosion rate as compared to Ti-40Nb alloy, evidenced by higher R_{ox} and lower i_{pass} values. This better behavior of Ti-25Nb-5Fe alloy may be linked with the fully diffused Nb and obtaining a fully β phase structure. However,

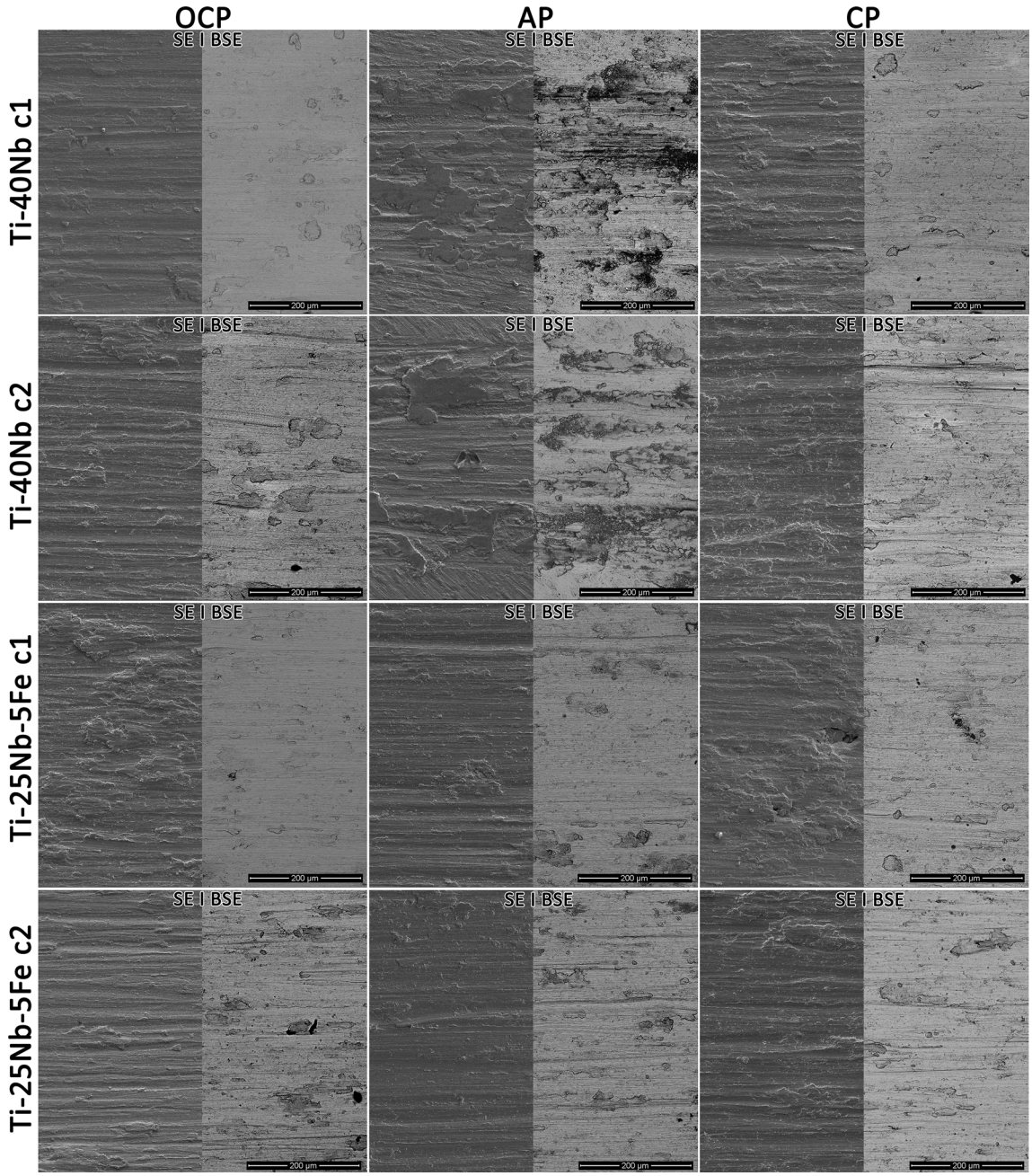

Fig. 8—SE- and BSE-SEM images of wear tracks for Ti-40Nb c1, Ti-40Nb c2, Ti-25Nb-5Fe c1, and Ti-25Nb-5Fe c2 of the samples tested under OCP, AP, and CP.

incorporation of iron oxides to the passive film of Ti-25Nb-5Fe alloy may also influence the corrosion behavior that needs further investigations by XPS analysis before and after corrosion tests.

Samples processed under c2 condition showed higher corrosion resistance than samples processed under the c1 condition for both alloys, evidenced by lower i_{pass}, lower C_{ox}, and higher phase angle values, which indicates lower corrosion rate and higher quality of passive film. Guo *et al.*[26] studied the influence of sintering temperature and sintering time on microstructure, mechanical properties, and electrochemical response of β-type Ti-24Nb-4Zr-7.9Sn alloy. The authors found that sintering at 1250 °C for 2 hours yielded with higher corrosion resistance in simulated body environments due to the transformation of the α phase to β phase and due to lower porosity. Tamilselvi and Rajendran[30] studied corrosion behavior of Ti-5Al-2Nb-1Ta alloy immersed in Hanks' solution for 0, 120, 240, and 360 hours using EIS test. Also, Alves *et al.*[31] investigated the electrochemical behavior Ti and Ti6Al-4V alloy immersed in Hanks' solution for 5 minutes, 24 hours and 7 days tested by the same technique. Both investigations reported that the n values were related to the non-uniform current distribution as a consequence of surface roughness or inhomogeneity.

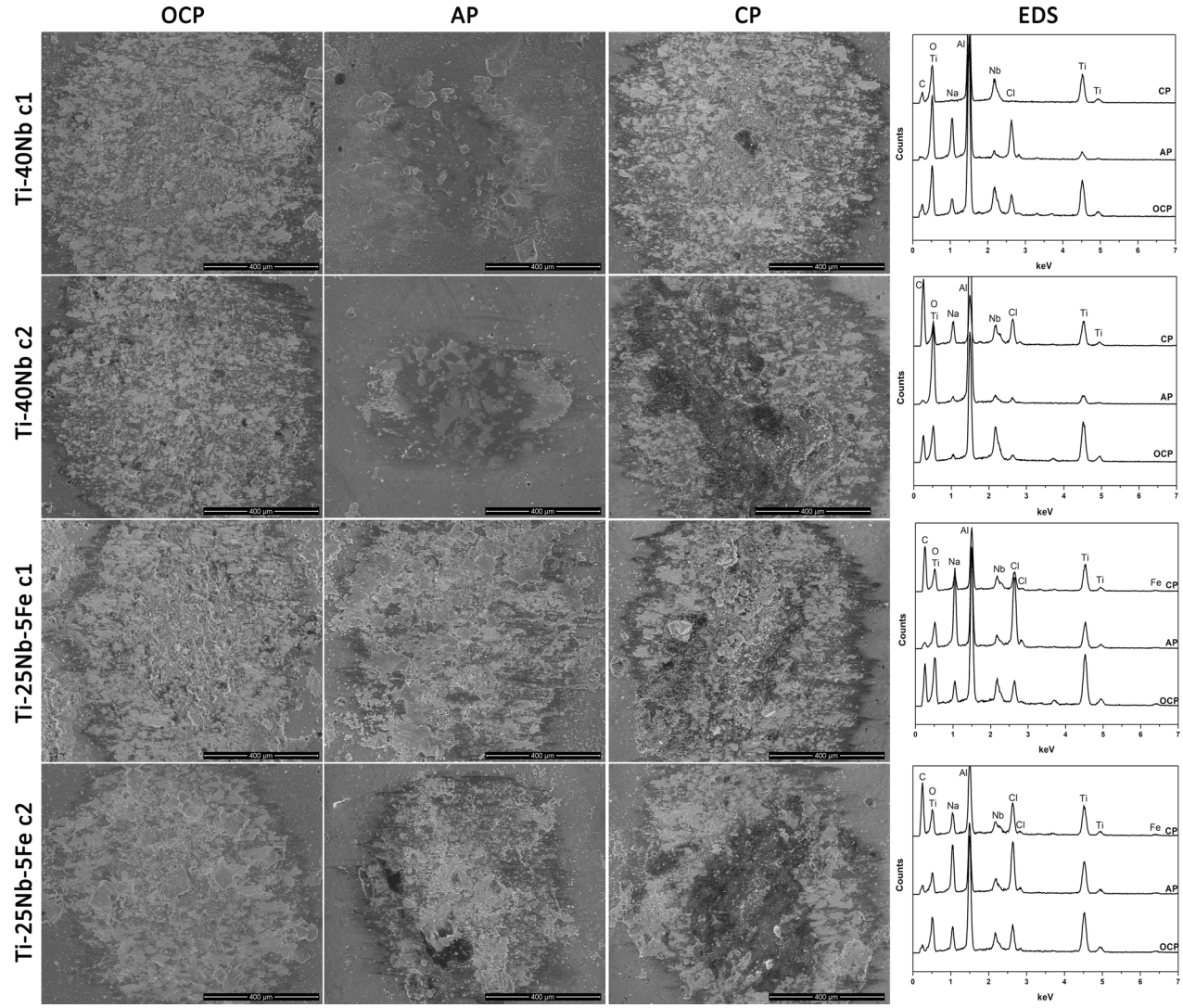

Fig. 9—SE-SEM images and respective EDS spectra of the alumina ball surfaces worn against Ti-40Nb c1, Ti-40Nb c2, Ti-25Nb-5Fe c1, and Ti-25Nb-5Fe c2 tested under OCP, AP, and CP.

Therefore, the better quality of the passive film obtained for both alloys produced under c2 condition may be explained by increased n values indicating a better phase distribution, thus, improved homogeneity.

C. *Tribocorrosion Behavior*

Thermodynamic tendency to corrosion under sliding can be evaluated through the evolution OCP values. Although no clear trend was observed between the testing groups when considering the results together with the standard deviation, alloys produced under c2 condition presented slightly higher average E_{OCP} values indicating lower tendency to corrosion that may be linked with the improved surface homogeneity.

Generally, wear loss under tribocorrosion conditions occurs through several mechanisms: wear accelerated corrosion (W_{wac}), mechanical wear (W_{mec}), and corrosion (W_{cor}). As Landolt *et al.*[32] demonstrated, the W_{cor} can be neglected in case of passive materials, thus the overall wear volume loss (W_{tot}) is expressed as the sum of W_{wac} and W_{mec}.

Mischler *et al.*[33] investigated the role of passive oxide films on carbon steel sliding against alumina ball and reported that the total wear volume loss of passive alloys in tribocorrosion system at AP condition resulted in combined influences of corrosion and wear, while the total wear volume loss in CP condition is attributed to mechanical wear (without the influence of corrosion). Usually, as reviewed by Cao and Mischler,[34] the wear volume loss in AP conditions is expected to be higher than those in CP and OCP conditions due to the synergistic interplay between corrosion and wear. However, the average wear volume losses on Ti-25Nb-5Fe alloy were similar after testing under OCP, AP, and CP, suggesting that the degradation process was mainly governed by mechanical wear. Regarding Ti-40Nb alloy, the average wear volume loss in AP condition was significantly lower as compared to the ones obtained on CP and OCP conditions, indicating an antagonistic

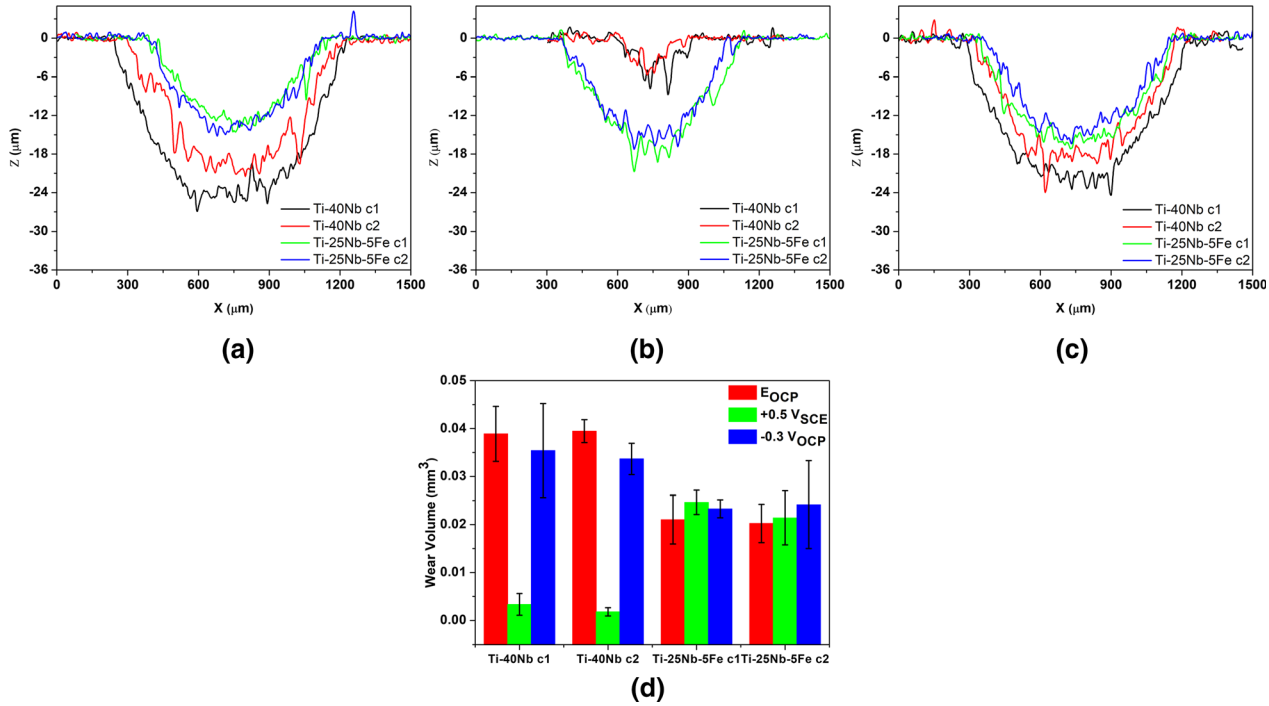

Fig. 10—Representative 2D wear track profiles of samples for testing at (*a*) OCP, (*b*) AP, (*c*) CP conditions, and (*d*) wear volume loss values.

effect between corrosion and wear. This was most probably due to the area covered by the discontinuous tribolayer that was substantially increased on Ti-40Nb alloys tested under AP, that played a protective role against tribocorrosion, evidenced with lower current density under sliding, lower COF, lower Q, and lower wear volume loss. Relatively lower corrosion resistance of Ti-40Nb, more specifically its lower R_{ox} and higher i_{pass} (*i.e.*, higher corrosion kinetics) may lead to the formation of a denser tribolayer during repetitive disturbance of the passive film under AP condition. This denser tribolayer may give a protection against wear and corrosion, however, after reaching a certain thickness, may be removed by the counter-material resulting in a rapid increase on the current density values (Figure 7(a)). Afterward, the tribolayer starts to form itself again and consequently the current density values decrease near to the values obtained on the onset of the sliding. Nevertheless, the undiffused Nb may also play a role on this behavior that needs further understanding by performing XPS analysis before and after corrosion and tribocorrosion tests for understanding the variations on the chemical composition of the native oxide film. Besides, lower wear volume loss values obtained on Ti-25Nb-5Fe alloy tested under OCP and CP conditions, where the influence of the mechanical wear was more predominant as compared to AP condition, were most likely affected by the higher hardness of this alloy as compared to Ti-40Nb.

Microstructural and chemical analysis of the worn sample and the counter-material surfaces indicated that wear was mainly dominated by mixed abrasive/adhesive wear mechanism. However, it was evident by the characterization of the worn counter-material surfaces that the influence of the adhesive wear was significantly reduced for Ti-40Nb alloy tested at AP condition due to the reduced direct contact area between the testing alloy and the counter-material surfaces after formation of a denser tribolayer on the worn surface (Figure 9).

V. CONCLUSION

Corrosion and tribocorrosion behaviors of Ti-25Nb-5Fe and Ti-40Nb alloys processed by P/M were investigated in saline solution (9 g/L NaCl). Electrochemical studies showed that Ti-25Nb-5Fe alloy presented higher corrosion resistance than Ti-40Nb alloy and the corrosion resistance of both alloys improved with the improved surface homogeneity. Ti-25Nb-5Fe alloys did not present a considerable difference on the wear volume loss after tribocorrosion tests performed under OCP or under anodic and cathodic potentiostatic conditions, indicating that the dominant degradation mechanism was mechanical wear. However, Ti-40Nb alloy exhibited significantly lower wear volume loss after tribocorrosion tests performed at anodic potentiostatic conditions, pointing an antagonistic effect between wear and corrosion due to formation of a denser tribolayer on the worn surfaces.

ACKNOWLEDGMENTS

This work is supported by FCT with the reference Project UID/EEA/04436/2019, together with M-ERA--NET/0001/2015, as well, by MINECO (Spain) through

the program PCIN-2016-123 and the Ramón y Cajal Project RYC-2014-15014. I. Caha is grateful for the financial support through a Ph.D. Grant under the NORTE-08-5369-FSE-000012 Project.

REFERENCES

1. M. Niinomi and M. Nakai: *Int. J. Biomater.*, 2011, https://doi.org/10.1155/2011/836587.
2. N.J. Hallab, S. Anderson, M. Caicedo, A. Brasher, K. Mikecz, and J.J. Jacobs: *J. Biomed. Mater. Res. Part A*, 2005, vol. 74, pp. 124–40.
3. Y. Okazaki, Y. Ito, K. Kyo, and T. Tateishi: *Mater. Sci. Eng. A*, 1996, vol. 213, pp. 138–47.
4. Y. Bai, Y. Deng, Y. Zheng, Y. Li, R. Zhang, Y. Lv, Q. Zhao, and S. Wei: *Mater. Sci. Eng. C*, 2016, vol. 59, pp. 565–76.
5. M.A. Gepreel and M. Niinomi: *J. Mech. Behav. Biomed. Mater.*, 2013, vol. 20, pp. 407–15.
6. Z.Z. Fang, J.D. Paramore, P. Sun, K.S.R. Chandran, Y. Zhang, Y. Xia, F. Cao, M. Koopman, and M. Free: *Int. Mater. Rev.*, 2017, vol. 63, pp. 1–53.
7. M. Niinomi, M. Nakai, and J. Hieda: *Acta Biomater.*, 2012, vol. 8, pp. 3888–3903.
8. M. Niinomi: *Metall. Mater. Trans. A*, 2002, vol. 33, pp. 477–86.
9. M. Popa, J.M. Calderon Moreno, C. Vasilescu, S.I. Drob, E.I. Neacsu, A. Coer, J. Hmeljak, G. Zerjav, and I. Milošev: *Metall. Mater. Trans. A Phys. Metall. Mater. Sci.*, 2014, vol. 45, pp. 3130–43.
10. D.R.N. Correa, P.A.B. Kuroda, C.R. Grandini, L.A. Rocha, F.G.M. Oliveira, A.C. Alves, and F. Toptan: *Mater. Lett.*, 2016, vol. 179, pp. 118–21.
11. V.G. Pina, A. Dalmau, F. Devesa, V. Amigó, and A.I. Muñoz: *J. Mech. Behav. Biomed. Mater.*, 2015, vol. 46, pp. 59–68.
12. N.S. More, N. Diomidis, S.N. Paul, M. Roy, and S. Mischler: *Mater. Sci. Eng. C*, 2011, vol. 31, pp. 400–08.
13. M. Calin, A. Helth, J.J. GutierrezMoreno, M. Bönisch, V. Brackmann, L. Giebeler, T. Gemming, C.E. Lekka, A. Gebert, R. Schnettler, and J. Eckert: *J. Mech. Behav. Biomed. Mater.*, 2014, vol. 39, pp. 162–74.
14. A. Helth, P.F. Gostin, S. Oswald, H. Wendrock, U. Wolff, U. Hempel, S. Arnhold, M. Calin, J. Eckert, and A. Gebert: *J. Biomed. Mater. Res. Part B Appl. Biomater.*, 2014, vol. 102, pp. 31–41.
15. J.M. Chaves, O. Florêncio, P.S. Silva, P.W.B. Marques, and C.R.M. Afonso: *J. Mech. Behav. Biomed. Mater.*, 2015, vol. 46, pp. 184–96.
16. P. Mohan, A.B. Elshalakany, T.A. Osman, V. Amigo, and A. Mohamed: *J. Alloys Compd.*, 2017, vol. 729, pp. 1215–25.
17. H.C. Hsu, S.K. Hsu, S.C. Wu, C.J. Lee, and W.F. Ho: *Mater. Charact.*, 2010, vol. 61, pp. 851–58.
18. S. Ehtemam-Haghighi, K.G. Prashanth, H. Attar, A.K. Chaubey, G.H. Cao, and L.C. Zhang: *Mater. Des.*, 2016, vol. 111, pp. 592–99.
19. S. Virtanen, I. Milošev, E. Gomez-Barrena, R. Trebše, J. Salo, and Y.T. Konttinen: *Acta Biomater.*, 2008, vol. 4, pp. 468–76.
20. E.K. Ocran, L.E. Guenther, J.M. Brandt, U. Wyss, and O.A. Ojo: *Metall. Mater. Trans. A Phys. Metall. Mater. Sci.*, 2015, vol. 46, pp. 2696–2709.
21. C. Chirico, S. Tsipas, F. Toptan, and E. Gordo: *Powder Metall.*, 2019, vol. 62, pp. 44–53.
22. D.C. Rodrigues, R.M. Urban, J.J. Jacobs, and J.L. Gilbert: *J. Biomed. Mater. Res. Part B Appl. Biomater.*, 2009, vol. 88B, pp. 206–19.
23. Z. Doni, A.C. Alves, F. Toptan, J.R. Gomes, A. Ramalho, M. Buciumeanu, L. Palaghian, and F.S. Silva: *Mater. Des.*, 2013, vol. 52, pp. 47–57.
24. J.I. Silva, A.C. Alves, A.M. Pinto, and F. Toptan: *J. Mech. Behav. Biomed. Mater.*, 2017, vol. 74, pp. 195–203.
25. M.J. Runa, M.T. Mathew, and L.A. Rocha: *Tribiol. Int.*, 2013, vol. 68, pp. 85–93.
26. S. Guo, A. Chu, H. Wu, C. Cai, and X. Qu: *J. Alloys Compd.*, 2014, vol. 597, pp. 211–16.
27. B. Sharma, S.K. Vajpai, and K. Ameyama: *J. Alloys Compd.*, 2015, vol. 656, pp. 978–86.
28. M. Niinomi, T. Akahori, S. Katsura, K. Yamauchi, and M. Ogawa: *Mater. Sci. Eng. C*, 2007, vol. 27, pp. 154–61.
29. E. John: *Oxford Univ. Press.* ISBN: 978-0-19-960563-7.
30. S. Tamilselvi and N. Rajendran: *Mater. Corros.*, 2007, vol. 58, pp. 285–89.
31. V.A. Alves, R.Q. Reis, I.C.B. Santos, D.G. Souza, M.A. Pereira-da-Silva, A. Rossi, and L.A. da Silva: *Corros. Sci.*, 2009, vol. 51, pp. 2473–82.
32. D. Landolt, S. Mischler, M. Stemp, and S. Barril: *Wear*, 2004, vol. 256, pp. 517–24.
33. S. Mischler, A. Spiegel, and D. Landolt: *Wear*, 1999, vols. 225–229, pp. 1078–87.
34. S. Cao and S. Mischler: *Curr. Opin. Solid State Mater. Sci.*, 2018, vol. 1, pp. 1–15.